electronics

MDPI

Article

Ternary Polymer Solar Cells: Impact of Non-Fullerene Acceptors on Optical and Morphological Properties

Quentin Eynaud [1], Tomoyuki Koganezawa [2], Hidehiro Sekimoto [3], Mohamed el Amine Kramdi [1], Gilles Quéléver [1], Olivier Margeat [1], Jörg Ackermann [1], Noriyuki Yoshimoto [3] and Christine Videlot-Ackermann [1,*]

[1] Aix-Marseille University, CNRS, CINAM, 13007 Marseille, France; quentin.eynaud@etu.univ-amu.fr (Q.E.); mohamed-el-amine.kramdi@etu.univ-amu.fr (M.e.A.K.); gilles.quelever@univ-amu.fr (G.Q.); olivier.margeat@univ-amu.fr (O.M.); jorg.ackermann@univ-amu.fr (J.A.)
[2] Industrial Application Division, Japan Synchrotron Radiation Research Institute (JASRI), Hyogo 679-5198, Japan; koganeza@spring8.or.jp
[3] Department of Physical Science and Materials Engineering, Iwate University, Morioka 020-8551, Japan; hidehiro@iwate-u.ac.jp (H.S.)
* Correspondence: christine.videlot-ackermann@cnrs.fr

Abstract: Ternary organic solar cells contain a single three-component photoactive layer with a wide absorption window, achieved without the need for multiple stacking. However, adding a third component into a well-known binary blend can influence the energetics, optical window, charge carrier transport, crystalline order and conversion efficiency. In the form of binary blends, the low-bandgap regioregular polymer donor poly(3-hexylthiophene-2,5-diyl), known as P3HT, is combined with the acceptor $PC_{61}BM$, an inexpensive fullerene derivative. Two different non-fullerene acceptors (ITIC and eh-IDTBR) are added to this binary blend to form ternary blends. A systematic comparison between binary and ternary systems was carried out as a function of the thermal annealing temperature of organic layers (100 °C and 140 °C). The power conversion efficiency (PCE) is improved due to increased fill factor (FF) and open-circuit voltage (V_{oc}) for thermal-annealed ternary blends at 140 °C. The transport properties of electrons and holes were investigated in binary and ternary blends following a Space-Charge-Limited Current (SCLC) protocol. A favorable balanced hole–electron mobility is obtained through the incorporation of either ITIC or eh-IDTBR. The charge transport behavior is correlated with the bulk heterojunction (BHJ) morphology deduced from atomic force microscopy (AFM), contact water angle (CWA) measurement and 2D grazing-incidence X-ray diffractometry (2D-GIXRD).

Keywords: ternary organic solar cells; non-fullerene acceptors; bulk heterojunction; thermal annealing; molecular order; charge transport

Citation: Eynaud, Q.; Koganezawa, T.; Sekimoto, H.; Kramdi, M.e.A.; Quéléver, G.; Margeat, O.; Ackermann, J.; Yoshimoto, N.; Videlot-Ackermann, C. Ternary Polymer Solar Cells: Impact of Non-Fullerene Acceptors on Optical and Morphological Properties. *Electronics* **2024**, *13*, 1752. https://doi.org/10.3390/electronics13091752

Academic Editors: Zhuoran Wang and Ying Li

Received: 6 April 2024
Revised: 28 April 2024
Accepted: 30 April 2024
Published: 2 May 2024

1. Introduction

The active layer of bulk heterojunction (BHJ) organic solar cells (OSCs), which is widely used, comprises two organic semiconductors, the electron donor and the electron acceptor blended in a common solvent at various D:A ratios [1–4]. A promising way of improving the efficiency of this type of solar cell is to incorporate a third component into the active layer to form a ternary heterojunction-based OSC [5]. The devices then contain a single three-component photoactive layer without the need for multiple stacking. The host system contains one donor (D or D_1) and one acceptor (A or A_1); meanwhile, the third component has the minority ratio in the blend and is defined as the guest. Depending on the nature of this third organic material (a secondary donor D_2 or a secondary acceptor A_2), the ternary heterojunction is defined as D_1:D_2:A or D:A_1.A_2. The benefits of integrating a third component can be varied and ideally cumulated as an improved spectral response with more overlap with the solar spectrum, more efficient charge transfer and a better-adapted morphology of the active layer, for a higher power conversion efficiency (PCE) [6–12].

As a binary blend, the well-studied model polymer/fullerene solar cell is the ideal host system. In the majority of cases, the blend is formed via the regioregular conjugated semiconducting polymer poly(3-hexylthiophene-2,5-diyl), P3HT [13,14], and the commonly used electron acceptor [6,6]-phenyl-C61-butyric-acid-methyl ester, $PC_{61}BM$. P3HT is simple in terms of chemical structure, remains the most popular donor polymer in organic photovoltaic (OPV) cells, and is low-cost compared to polymers with complex structures needing multiple synthesis steps with relatively low yields. Moreover, $PC_{61}BM$ is characterized by a well-established and comparably cheap synthesis platform. The commercial availability of these two compounds keeps them highly attractive to the research community. Thus, despite significantly higher device efficiencies in other D:A blend systems, the traditional P3HT:$PC_{61}BM$ system can still have some relevance in practical applications.

Fullerene derivative acceptors were initially the only candidate acceptors and absorbed only in the high-energy region of the visible spectrum, leaving a large absorption window at lower energies. New acceptor materials named non-fullerene acceptors (NFAs) have established themselves as serious competitors to fullerenes as electron-acceptor materials for OPV devices [15–17]. The rise of NFAs resulted in the quick development of molecules such as ITIC and IDTBR families (see Figure 1 for chemical structures and the Supplementary Materials for chemical names) [15,18]. The energy levels of the NFAs can be adjusted by modifying the conjugated skeletons. In addition, the solubility and morphology of NFA mixtures can be controlled via side-chain engineering and their bandgap (Eg) can be adjusted to harvest photons in a region of the solar spectrum complementary to the donor's absorption region. Nevertheless, the NFA introduced as the third organic material in ternary OSCs must have band energy levels with the energy levels of the donor and acceptor. In addition, its presence should not negatively affect the morphology of the binary blend in terms of crystallinity, molecular orientation and nano-phase separation between the donor and acceptor of the host system.

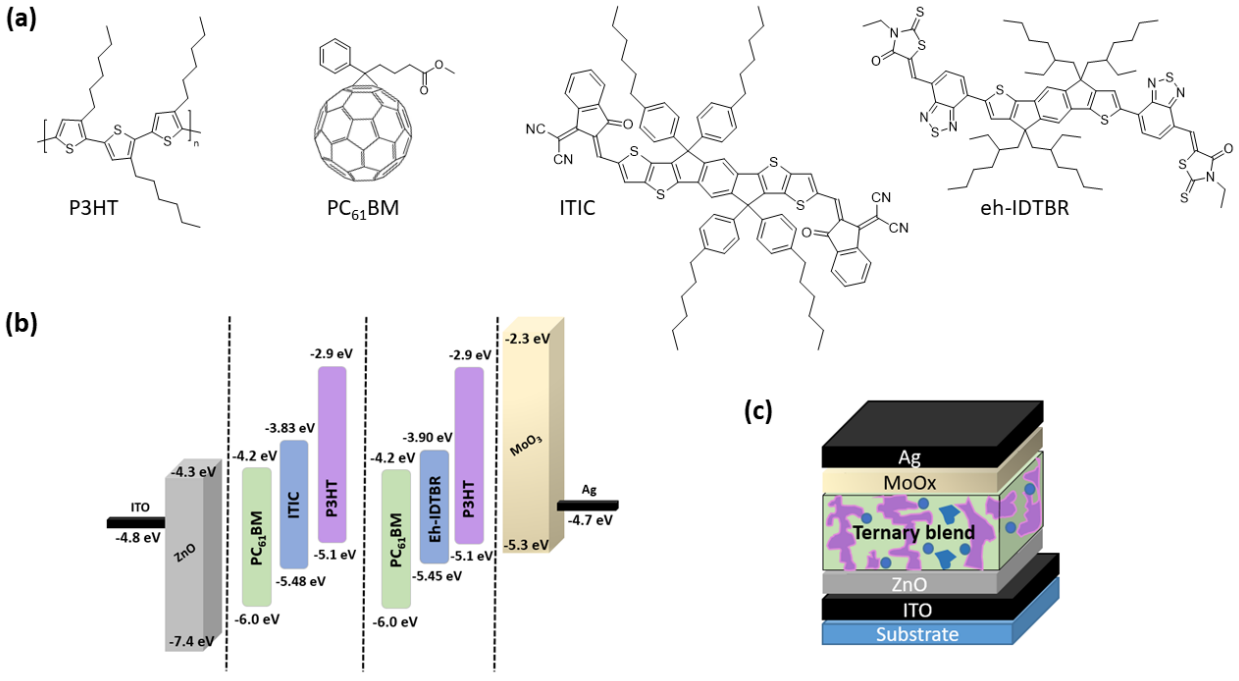

Figure 1. Chemical structure of materials (**a**), energy diagram of ternary blend-based OPVs in inverted structure (**b**), schematic diagram of inverted structure (**c**).

In this work, optical, photovoltaic and morphological properties are investigated for ternary solar cells containing a traditional P3HT:$PC_{61}BM$ BHJ active layer modified with the incorporation of a third NFA-based component, e.g., ITIC or eh-IDTBR. A systematic comparison between binary and ternary blends was carried out as a function of

the thermal annealing temperature of the organic layer (100 °C and 140 °C). The first feature is a long-wave detection range of the P3HT:PC_{61}BM host system over 650 nm via the generation of a new absorption peak at 700 nm due to the contribution of the third NFA-based component. Through the addition of 15 wt% of NFA in a final weight ratio of 0.85:1:0.15 for P3HT:PC_{61}BM:NFA ternary BHJ, the contribution of NFA to spectral conversion efficiency towards wavelengths beyond 650 nm is promoted. This substantial efficiency enhancement is attributed to the role of NFAs in improving light absorption over a wavelength range of 650 nm in combination with better matching of the energy levels of the ternary blend system. The morphology of binary and ternary blends is studied in detail with atomic force microscopy (AFM), contact water angle (CWA) measurements and 2D grazing-incidence X-ray diffractometry (2D-GIXRD). A good incorporation of NFA molecules to form an amorphous mixed phase with PC_{61}BM is highlighted. At 140 °C, very distinct characteristics are displayed. The inclusion of NFAs increases the crystallinity of P3HT with more ordered crystallite formation. P3HT-enriched domains being the charge transport matrix for the positive carriers, the transport of holes determined by the Space-Charge-Limited Current (SCLC) protocol is strengthened. This increase in hole mobilities is coupled with higher electron mobility in ternary blends annealed at 140 °C. In the case of P3HT:PC_{61}BM:eh-IDTBR blends, CWA reveals the formation of a layer enriched in P3HT on the top surface of the blend, which is favorable for the extraction of holes in an inverted OPV structure. This morphology, combined with balanced mobility between holes and electrons, enables charges to be efficiently generated and transported in the corresponding solar cells. Increased performances were obtained with ternary blends at 140 °C due to higher V_{oc} and better FF. The highest efficiency was obtained for P3HT:PC_{61}BM:eh-IDTBR blends annealed at 140 °C.

2. Materials and Methods

Materials. Patterned ITO substrates (size 25 mm × 25 mm) with 15 Ω/sq resistance were purchased from Lumtec, Taiwan. A 2.5%vol. ZnO nanoparticle solution in an alcohol blend ZnO was purchased from Avantama and diluted to 1%vol. before use. Orthodichlorobenzene (ODCB) solvent, molybdenum (VI) oxide (MoO_3, purity 99.97%) and lithium fluoride (LiF, purity ≥ 99.99%) were purchased from Sigma-Aldrich; ITIC and eh-IDTBR were purchased from 1-Material; PEDOT:PSS (Al 4083) and P3HT (RR 93.6%, M_w 24.48, M_n 8.75, PDI 2.8) were purchased from Ossila; PC_{61}BM was purchased from Nano-C and silver (Ag, purity 99.99%) was purchased from Kurt J. Lesker. All commercial materials were used as received without purification and kept under a nitrogen atmosphere.

Ink preparation. Binary solution was prepared in ODCB without additives at a 1:1 weight ratio to reach a final concentration of 55 mg.mL^{-1}. Ternary solutions (P3HT:PC_{61}BM:ITIC and P3HT:PC_{61}BM:eh-IDTBR) were prepared with the same final concentration of 55 mg.mL^{-1} in a weight ratio of 0.85:1:0.15 in ODCB without additives. The inks were stirred at 85 °C overnight. Binary and ternary solutions were spin-coated inside a nitrogen-filled glovebox at 1000 rpm for 60 s followed by a post-deposition thermal annealing at 100 °C or 140 °C for 10 min. The average layer thickness of binary and ternary layers is ~200 nm.

Solar cell fabrication and characterizations. The solar cells were fabricated in an inverted (ITO/ZnO/BHJ/MoO_3/Ag) structure on ITO-coated glasses using a spin-coating technique in a glovebox under a nitrogen atmosphere. First, the ITO substrates were thoroughly cleaned with a clean cloth dampened with isopropanol before sonication in isopropanol for 30 min and the application of UV ozone for 15 min at 80 °C. A thin layer of ZnO was spin-coated on the cleaned ITO substrate in the ambient conditions at a speed of 5000 rpm for 60 s followed by an annealing step inside a nitrogen-filled glovebox at 100 °C for 10 min to form a 15 nm thick film. After BHJ deposition, MoO_3 and Ag were successively thermally evaporated at 2 × 10^{-6} mbar to 2 nm and 100 nm thick layers, respectively, using a shadow mask to obtain device areas of 0.09 cm^2 and 0.25 cm^2.

The current density–voltage characterizations of the devices under an AM1.5G light solar simulator (Newport Sol3A Class AAA) were recorded with a Keithley 238 source

meter unit inside the glovebox. The illumination intensity of the light source was calibrated to be 100 mW/cm^2 using a standard silicon solar cell (Newport Company, Oriel no. 94043A) calibrated by the National Renewable Energy Laboratory (NREL). Values are based on an average of 6 devices.

External quantum efficiency (EQE) measurements were processed in a dark room in ambient conditions with a 150 W Xe arc lamp Apex illuminator (70525) light source collimated to a Cornerstone™ 260 1/4m UV-VIS Monochromator (74125) from Oriel Instruments for the light part and with a Keithley 238 Source Measure Unit for the electrical part. Devices were mounted on an optical table in a Faraday cage with an aperture to expose the samples to the monochromatic light. The electrodes of the devices were electrically connected to the cage with spring-loaded pogo pin connectors. The light beam was filtrated with 295 nm (10CGA-295) and 570 nm (10CGA-570) long-pass filters before reaching the devices.

Fabrication and measurements of Space-Charge-Limited Current devices. Space-Charge-Limited Current (SCLC) devices require the careful choice of the contacts to ensure a sufficient injection of the desired carrier, and an effective blocking of the other carrier to work like single-carrier devices [19–21]. Hole-only and electron-only devices consisted of ITO/PEDOT:PSS/BHJ/MoO_3/Au and ITO/ZnO/BHJ/LiF/Al, respectively. In SCLC-based devices, the mobility is measured vertically in the entire bulk of the active layer sandwiched between the two interfacial layers. Top metallic electrodes were thermally evaporated (MBRAUN evaporator inside the glovebox) at 2×10^{-6} mbar to a controlled thickness (13 nm of MoO_3, 100 nm of Au, 0.5 nm of LiF and 100 nm of Al) using a shadow mask that defines the device areas to 0.09 cm^2 or 0.25 cm^2 and allows a four-probe measurement. SCLC four-probes measurements were performed in the same Faraday cage as for OPVs inside the glovebox. The inks were deposited through spin-coating at 1000 rpm for 60 s. Active layers were subsequently annealed at 100 °C or 140 °C during 10 min.

The measured dark current was fitted using the Murgatroyd expression:

$$I = A\mu_0 \frac{9}{8} \frac{V^2}{d^3} \varepsilon\varepsilon_0 \exp\left(0.891\gamma\sqrt{\frac{V}{d}}\right) \quad (1)$$

where d is the active layer thickness; A is the active device area; $\varepsilon\varepsilon_0$ is the permittivity of the active layer (ε is assumed equal to 3.5 and ε_0 is the permittivity of free space); V is the voltage; μ_0 and γ are the unknown parameters that will be adjusted to obtain a good fit, all other parameters are fixed [22]; μ_0 is the mobility at low electric fields and γ is a parameter that represents the field dependence of mobility.

Characterization of Organic films. The absorbance of the active layer films was measured via a UV–Vis–near infrared Spectrophotometer Cary 5000. The surface morphology of the blend layers was investigated via AFM (NTEGRA from NT-MIDT) in semi-contact mode using the silicon tips (MikroMash) with a theoretical resonant frequency of 150 kHz and a force constant of 5.4 N.m^{-1} at room temperature. Film thicknesses were measured using a stylus profilometer (Bruker DEKTAK XT) with 1 mg of force on the probing tip. Contact water angle (CWA) measurements were performed with an optical contact angle (OCA) series 15EC with a high-resolution USB camera and sample positioning from DataPhysics Instrument GmbH Company in a room with a controlled temperature at 20 °C.

Thin films were further analyzed with high-brightness synchrotron radiation at BL19B2 in SPring-8 (Sayo in Japan). GIWAXS (Grazing-Incidence Wide-Angle X-ray Scattering) measurements were performed using a high-sensitive 2D X-ray detector (PILATUS 300K). The incident angle and wavelength of X-rays were 0.13° and 0.100 nm, respectively. The crystal coherence length (CCL) values were extracted via the Scherrer equation:

$$\tau = \frac{K\lambda}{\beta\cos\theta} \quad (2)$$

where τ is the ordered (crystalline) domains (which may be smaller or equal to the grain size), here defined as CCL; K is a constant (dimensionless shape factor) closed to unity, and the shape factor is typically equal to 0.9; λ is the wavelength of the X-ray; β is the full width at half maximum (FWHM) of the diffraction peak in radians after subtracting the instrumental line broadening and θ is the Bragg angle. From an analytical standpoint, FWHM is used to determine the length scale over which ordered regions (e.g., crystallites) diffract/scatter coherently via the Scherrer equation.

3. Results

Figure 1a,b show the chemical structures of P3HT, $PC_{61}BM$, ITIC and eh-IDTBR and their energy levels. The lowest unoccupied molecular orbital (LUMO) and the highest occupied molecular orbital (HOMO) levels of P3HT, ITIC, eh-IDTBR and $PC_{61}BM$ follow a normative cascade alignment, indicating the potentially efficient charge transport path between them. ZnO and MoO_3 are used as electron and hole extraction layers, respectively, in an inverted OPV structure (Figure 1c).

3.1. Impact of the Third Component on Absorption Spectra

Photon harvesting is the main key issue to obtain high performance in polymer solar cells. Figure 2a,b depict the UV–Vis absorption spectra of neat films (P3HT, $PC_{61}BM$, ITIC and eh-IDTBR) compared to the AM1.5 standard solar spectra. $PC_{61}BM$ films absorb the short wavelength with its maximum at 335 nm together with a relatively lower absorbance in the visible between 400 and 600 nm. P3HT can utilize light in the middle wavelength from 450 nm to 650 nm. The NFA acceptors, ITIC and eh-IDTBR, can realize the absorption from 550 nm to 800 nm. Evidently, these three active layer materials complement each other well in the visible spectrum. Therefore, the ternary blend films have an excellent potential to realize full visible photodetection. In Figure 2c,d, the absorption spectra of both ternary blends (P3HT:$PC_{61}BM$:ITIC and P3HT:$PC_{61}BM$:eh-IDTBR) are presented as a function of annealing temperature. P3HT:$PC_{61}BM$ films show favorable light absorption capacity from 400 nm to 600 nm, but there is almost no absorption in the long-wave region after 600 nm. After introducing ITIC or eh-IDTBR, a new absorption peak is generated at 700 nm due to the contribution of the third NFA-based component, which extends the long-wave detection range of the P3HT:$PC_{61}BM$ host system. With a 0.85:1:0.15 ratio for P3HT:$PC_{61}BM$:ITIC and P3HT:$PC_{61}BM$:eh-IDTBR ternary blends, reducing the wt% of P3HT balances the absorption intensity, which is evidently beneficial for equilibrating the photodetection in short and long wavelengths simultaneously, and realizing the broadband OPVs with full photodetection in the visible.

In order to remove the solvent molecules after the spin-coating process, we applied a post-annealing treatment at 100 °C or 140 °C for 10 min on the organic layers. The post-deposition treatment at a higher temperature of 140 °C is intended to finalize the drying process and the reorganization of molecules in thin films. P3HT and $PC_{61}BM$ both exhibit a high melting temperature (Tm) and crystallization temperature (Tc) (P3HT: Tm = 233 °C and Tc = 194 °C [23]; $PC_{61}BM$: Tm = 249 °C and Tc = 285 °C [24]). With a ratio of 0.85:1:0.15, the ternary blend mainly contains P3HT and $PC_{61}BM$, enabling no degradation of the studied films to occur at 140 °C and only a reorganization of the molecules inside the films can proceed. The absorption spectra of neat films depending on annealing temperature are depicted in Figure S1. Among all neat materials, P3HT displays the greatest impact of thermal annealing (see Table S1). At 140 °C, the absorption spectrum of P3HT centered at 552 nm is more intense with its shoulders clearly visible at 520 and 608 nm. For $PC_{61}BM$ and ITIC, the effect of annealing has very little influence on absorption spectra in terms of intensity, without significant wavelength shift. A special feature is observed for eh-IDTBR with an inverse impact of thermal annealing (see the comments with Figure S1 and Table S1). It is important to note, however, that while no effect of annealing was apparent in the absorption spectra of the binary P3HT:$PC_{61}BM$ blends (Figure S2), P3HT polymer chains reorganize themselves again through the incorporation of NFAs as a third component in

ternary BHJs annealed at 140 °C (Figure 2c,d). In these ternary layers annealed at 140 °C, the contribution of $PC_{61}BM$ at 335 nm and NFA at 700 nm remains unchanged, suggesting only an induced arrangement of P3HT chains through the joint contribution of a third component and thermal annealing. With a higher absorption ability at 140 °C, ternary blends are expected to deliver OPVs with increased conversion efficiency.

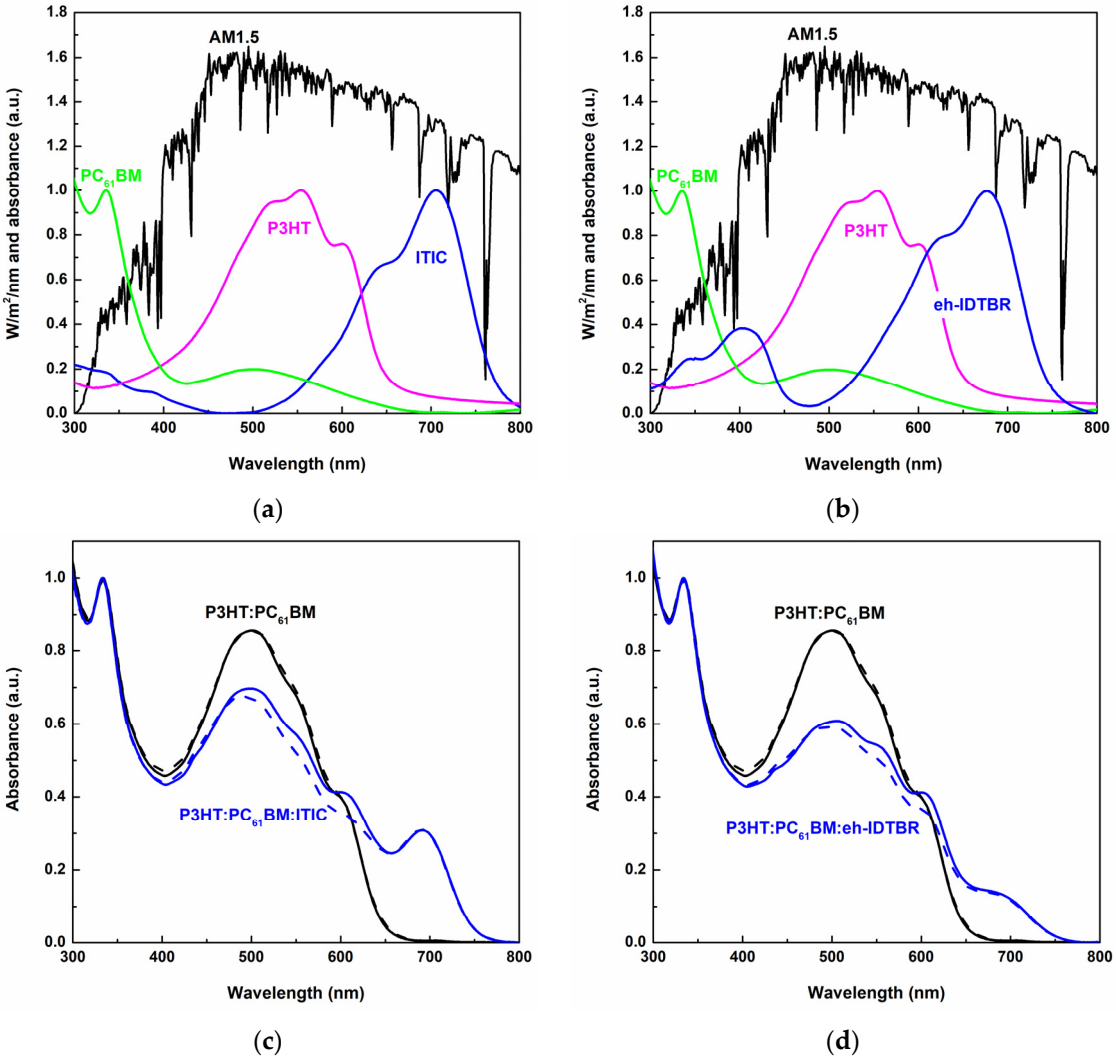

Figure 2. (**a**,**b**) Normalized UV–Vis absorption spectra of neat materials in thin films compared to AM1.5 for the standard solar spectrum emitted by the sun with an integrated power of 1000 W/m^2 (100 mW/cm^2). Normalized UV–Vis absorption spectra of ternary P3HT:PC_{61}BM:ITIC (**c**) and P3HT:PC_{61}BM:eh-IDTBR (**d**) blends compared to binary P3HT:PC_{61}BM blend. BJHs were thermally annealed at 100 °C (dotted line) or 140 °C (solid line).

3.2. Impact of the Third Component on Solar Cell Efficiency

To investigate the photovoltaic properties of the ternary active layer, we fabricated OSCs using an inverted device structure, ITO/ZnO/BHJ/MoO_3/Ag (Figure 1c). A systematic comparison to a binary system is realized as a reference. Identical final concentrations (55 $mg.mL^{-1}$) and deposition conditions (spin-coating at 1000 rpm for 60 s) between binary and ternary systems produce films of comparable thickness (see Table S2). Table 1 summarizes the photovoltaic parameters in terms of open-circuit voltage (V_{oc}), charge current density (J_{sc}), fill factor (FF) and power conversion efficiency (PCE). Figure 3 compares the current–density (J–V) curves of solar cells based on binary (P3HT:PC_{61}BM) and ternary (P3HT:PC_{61}BM:ITIC and P3HT:PC_{61}BM:eh-IDTBR) blends annealed at 140 °C. Regardless

of temperature, the ternary blends deliver a V_{oc} of 0.61–0.62 V, which is ~0.1 V higher than the binary component. This behavior can be explained via the higher LUMO energy level of ITIC and eh-IDTBR with that of $PC_{61}BM$, resulting in a larger energy offset with the HOMO of P3HT. This trend suggests the formation of an alloy-like mixed phase between NFAs (ITIC and eh-IDTBR) and P3HT donor polymer promoted via the very efficient incorporation of NFA molecules towards the D:A interface charge separation zone [25]. In addition, by forming an energy cascade alignment with the binary components, efficient charge extraction channels can be created and V_{oc} can be improved [26]. A significant effect of the annealing temperature of ternary blends is also visible on J_{sc}. Whereas a lower absorption leads to a lower J_{sc} for 100 °C, thermal annealing at 140 °C increases until Jsc is almost equal to that of the binary system. This increase can be the direct result of higher photon harvesting with the extended light absorption capacity in ternary blends. The third parameter, FF, also reveals a strong dependence on annealing temperature. An increase in FF value highlights a morphological evolution of the ternary blends during thermal annealing at 140 °C with a maximum value of 61.27% for P3HT:PC_{61}BM:eh-IDTBR. The fill factor is largely associated with resistances within the device, particularly at the electrode interfaces, and as such is highly influenced by the nanomorphology of these interfaces. Slightly better performances were obtained with ternary mixtures at 140 °C due to higher V_{oc} and better FF. The highest efficiency was obtained for P3HT:PC_{61}BM:eh-IDTBR blends annealed at 140 °C with a PCE value of 1.97%.

Table 1. Photovoltaic parameters of binary (P3HT:PC_{61}BM) and ternary (P3HT:PC_{61}BM:ITIC and P3HT:PC_{61}BM:eh-IDTBR) blends as a function of thermal annealing temperature.

Layer	Ratio	Temp. (°C)	V_{oc} (V)	J_{sc} (mA.cm^{-2})	FF (%)	PCE (%)	Integrated J_{sc} (mA.cm^{-2})
P3HT:PC_{61}BM	1:1	100	0.52	5.41	42.07	1.18	
		140	0.54	5.37	44.83	1.30	5.77
P3HT:PC_{61}BM:ITIC	0.85:1:0.15	100	0.62	3.55	43.05	0.95	
		140	0.61	5.17	57.55	1.82	5.11
P3HT:PC_{61}BM:eh-IDTBR	0.85:1:0.15	100	0.60	3.6	54.72	1.18	
		140	0.62	5.19	61.27	1.97	5.22

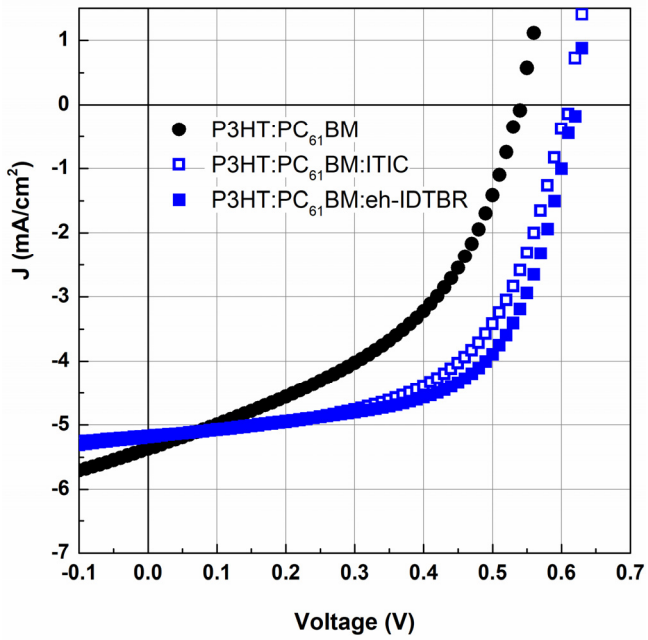

Figure 3. J–V curves of OPVs based on binary (P3HT:PC_{61}BM) and ternary (P3HT:PC_{61}BM:ITIC and P3HT:PC_{61}BM:eh-IDTBR) blends annealed at 140 °C.

By choosing to reduce the wt% of P3HT, which is highly absorbent in the visible range, we are favoring the contribution of NFA to spectral conversion efficiency towards wavelengths beyond 650 nm (Figure 4). The device based on binary P3HT:PC_{61}BM films shows a large and flat EQE peak covering the range of 300–650 nm attributed to the absorption of P3HT and PC_{61}BM. After introducing ITIC or eh-IDTBR into the P3HT:PC_{61}BM host system, the EQE curves of the broadband OPVs extend over 650 nm, and a new spectral peak from 650 nm to 750 nm is generated. EQE curves show that ternary OPVs effectively extend their continuous optical response by covering the entire visible light spectrum. In addition, a new spectral profile appears, with a peak centered at 550 nm and two marked shoulders on either side at 400 and 700 nm. According to the EQE curves, the synergy between the donor and acceptors at the ratio 0.85:1:0.15 balances the EQE over the entire wavelength. Integrated photoelectron current density J_{SC} values calculated from EQE data (Figure 4) and reported in Table 1 are consistent with the J_{SC} calculated from the J–V curves.

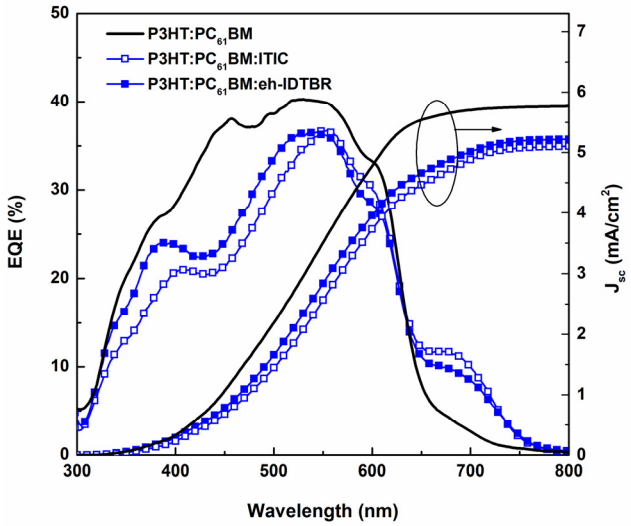

Figure 4. EQE spectra and integrated J_{sc} of OPVs based on ternary blends (P3HT:PC_{61}BM:ITIC and P3HT:PC_{61}BM:eh-IDTBR) compared to OPVs based on the binary P3HT:PC_{61}BM blend. BJHs were thermally annealed at 140 °C.

3.3. Impact of the Third Component on Charge Transport Properties

To investigate the influence of charge carrier transport properties through the introduction of NFAs, the SCLC model was adopted. The electron-only devices were fabricated with the structure of ITO/ZnO/BHJ/LiF/Al, and hole-only with ITO/PEDOT:PSS/BHJ/MoO_3/Au. According to Equation (1), the electron and hole mobility values determined with SCLC protocol for electron-only and hole-only devices based on P3HT, P3HT:PC_{61}BM, P3HT:PC_{61}BM:ITIC and P3HT:PC_{61}BM:eh-IDTBR layers as a function of thermal annealing temperature (100 °C or 140 °C) are summarized in Table S2. The thickness of each layer is indicated as required by the SCLC protocol, with comparable values around 200 nm. Figure 5a shows the evolution of electron and hole mobility values (μ_e, μ_h) and their ratio (μ_e/μ_h). Combined maximum values for electron and hole mobility are obtained for the ternary systems annealed at 140 °C with electron mobilities as high as 1.99×10^{-4} cm^2 V^{-1} s^{-1} and 4.13×10^{-4} cm^2 V^{-1} s^{-1} and hole mobilities of 5.14×10^{-3} cm^2 V^{-1} s^{-1} and 6.43×10^{-3} cm^2 V^{-1} s^{-1} for P3HT:PC_{61}BM:ITIC and P3HT:PC_{61}BM:eh-IDTBR, respectively. With the introduction of ITIC or eh-IDTBR, electron mobility increases by one order compared with the binary system, and hole mobility also increases, both reaching maximum values in ternary systems annealed at 140 °C. With electron mobility values as high as 0.01 and 0.05 cm^2 V^{-1} s^{-1} for ITIC and eh-IDTBR [27], respectively, increased μ_e values demonstrate the effective incorporation of NFA molecules into the enriched-acceptor phases. This incorporation is not effectless on enriched-donor domains as a higher hole transport is also measured. With μ_e/μ_h approaching 1, ternary

systems offer the balanced transport of photogenerated electrons and holes in blends, which contribute to higher PCE values obtained for ternary OPVs based on the 140 °C-annealed P3HT:PC_{61}BM:ITIC and P3HT:PC_{61}BM:eh-IDTBR blends.

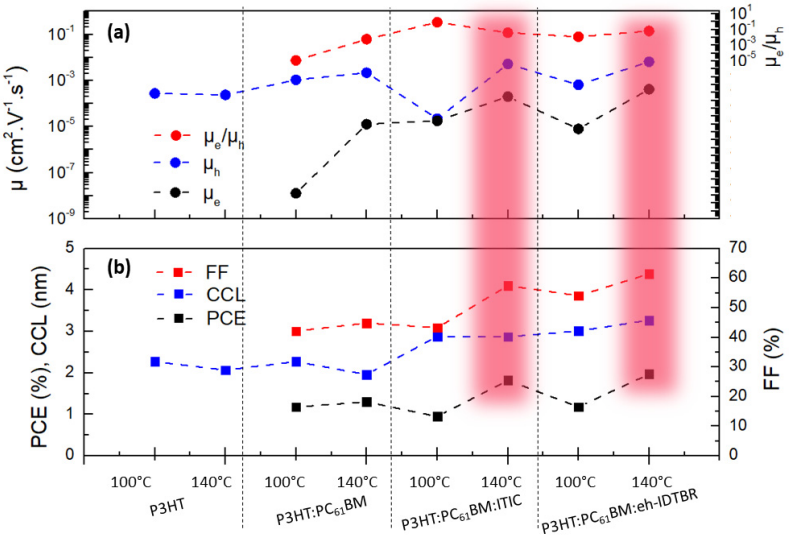

Figure 5. Evolution of electron and hole mobilities (μ_e, μ_h) and their ratio (μ_e/μ_h) (**a**), and FF, CCL and PCE (**b**) as a function of layers (neat PH3T, binary P3HT:PC_{61}BM blends, ternary P3HT:PC_{61}BM:ITIC blends and ternary P3HT:PC_{61}BM:eh-IDTBR blends) at 100 °C and 140 °C.

3.4. Impact of the Third Component on Molecular Ordering

To correlate the charge carrier mobility variation, especially at 140 °C, with structural changes in the molecular ordering of the layers, we combined a set of advanced techniques including AFM, WCA and GIWAXS to gain deeper structure–property relationships. Figure 6 compares the AFM images of the binary P3HT:PC_{61}BM and ternary P3HT:PC_{61}BM:eh-IDTBR layers annealed at 140 °C. AFM images of neat materials and P3HT:PC_{61}BM:ITIC blends are shown in Figure S3. According to the height image, the root-mean-square (rms) roughness values are summarized in Table 2. The surface of P3HT films is the roughest with an rms of about 3.3–3.35 nm. For each neat material, the rms value increases slightly at 140 °C, which may be due to molecular rearrangement caused by thermal annealing. Eh-IDTBR is the most sensitive material with an increasing rms value up to 1.16 nm at 140 °C versus 0.40 nm at 100 °C, accompanied by the appearance of structures lying outside the plane of the surface (Figure S3d). Films of binary and ternary blends are no exception to the trend, with a higher rms at 140 °C, but without any remarkable features at the resolution of the atomic force microscope. All binary and ternary blends have a granular surface topography and no phase separation.

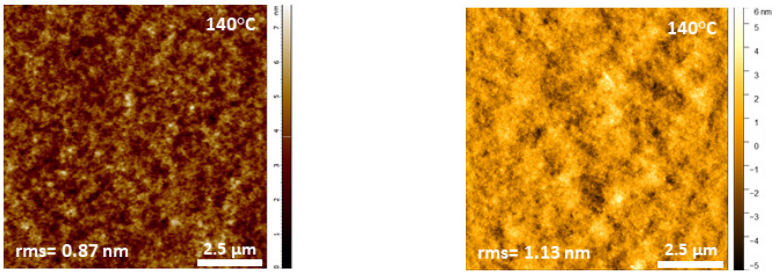

(**a**) (**b**)

Figure 6. AFM images of the binary P3HT:PC_{61}BM (**a**) and ternary P3HT:PC_{61}BM:eh-IDTBR (**b**) layers annealed at 140 °C.

Table 2. Water contact angle (WCA) and root-mean-squared roughness (rms) values for neat materials, binary and ternary blends as a function of thermal annealing temperature.

Layer	Ratio	T (°C)	rms (nm)	WCA (°)
P3HT		100	3.35	101.2
		140	3.30	103.0
$PC_{61}BM$		100	0.34	77.7
		140	0.43	74.4
ITIC		100	0.47	94.4
		140	0.86	92.2
eh-IDTBR		100	0.40	90.4
		140	1.16	49.5
P3HT:$PC_{61}BM$	1:1	100	0.76	92.7
		140	0.87	92.0
P3HT:$PC_{61}BM$:ITIC	0.85:1:0.15	100	1.31	90.9
		140	1.34	92.9
P3HT:$PC_{61}BM$:eh-IDTBR	0.85:1:0.15	100	0.99	103.5
		140	1.13	103.2

To provide information on the wettability evolution of the surface components of blend films, we realized WCA characterizations on neat materials and blends as a function of thermal annealing temperature (Figure S4 and Table 2). The WCAs of pure P3HT and $PC_{61}BM$ films were ~100° and ~75°, respectively, indicating that $PC_{61}BM$ has a relatively strong hydrophilic property [28]. The WCA of NFAs is slightly less (~90°) than P3HT as already reported [29,30]. It is worth noting that the WCA of eh-IDTBR films annealed at 140 °C differs, as with their rms, with a value divided by 2 suggesting a great change in surface morphology. As described by Wenzel's model [31], roughness can enhance both the hydrophobicity and hydrophilicity in the sense that the roughness makes a hydrophobic surface more hydrophobic, or more hydrophilic if the surface is originally hydrophilic. We can, therefore, assert here that the lower hydrophobicity of eh-IDTBR films at 140 °C is directly related to the morphology of their rough upper surfaces.

As expected, the WCA of binary P3HT:$PC_{61}BM$ blends is slightly less (~92°) than pure P3HT films due to the appearance of $PC_{61}BM$ on the top surface of blend films. This presence of fullerene molecules can also explain the lower surface roughness measured for the binary system compared to neat P3HT films. The component ratio of binary blends has been calculated using the Cassie–Baxter equation (see the details with Figure S4 in the Supplementary Materials). With the ratio doubled at 140 °C, the fraction of P3HT on the film surface increases substantially with annealing temperature, which implies a greater accumulation of polymer chains on the surface and higher PCE values in inverted OPVs (PCE increases from 1.18% to 1.30%; see Table 1). The most relevant result is obtained for ternary systems. The ternary system containing ITIC shows the same trends as the binary system, suggesting the excellent incorporation of ITIC molecules throughout the volume. By contrast, P3HT:$PC_{61}BM$:eh-IDTBR films have WCA values similar to those of P3HT. This observation suggests that incorporating eh-IDTBR induced the migration of P3HT molecules onto the upper surface. Although the Cassie–Baxter equation is not applicable to ternary blends, it can be assumed that this effect is in addition to the impact of annealing observed in the binary system. In the inverse OPV structure, where holes have to be extracted via the upper interfacial layer (here MoO_3), this P3HT-enriched surface contributes to a better hole extraction and, therefore, higher performances as effectively measured with an FF of 61.27% and a PCE of 1.97% for ternary P3HT:$PC_{61}BM$:eh-IDTBR-based OPVs annealed at 140 °C (see Table 1).

To probe the volume structural state of the blends, we performed 2D-GIXRD measurements on neat P3HT, binary and ternary blends. We probe molecular orientation (edge-on, face-on), intermolecular distances (d) and CCL (Table 3). Figure 7 shows the out-of-plane

(q_z) intensity profiles of ternary blends compared to the binary P3HT:PC_{61}BM layer. The corresponding 2D-GIXRD patterns as a function of thermal annealing temperature are depicted in Figure S5. In order to identify the contribution of either PC_{61}BM, ITIC or eh-IDTBR, neat layers were analyzed (Figures S6 and S7, see [32] for ITIC). The emergence of an intense, narrow diffraction peak indexed (100) at q_z = 0.39 $Å^{-1}$ and its replicas (200) and (300) in the q_z profile highlights that P3HT films are composed of highly ordered crystallites (Figure S8). It is attributed to the edge-on lamellar stacking of P3HT with a lattice constant (*d*-spacing) of 1.61 nm and a CCL calculated with Equation (2) of 2.07–2.24 nm. Blended in binary or in ternary films, the crystalline state of P3HT is conserved as observed by the predominant presence of the diffraction peaks (100) in the q_z profile (Figure 7). No characteristic peaks of ITIC or eh-IDTBR appear in blends, suggesting that acceptor molecules mix in amorphous phases with PC_{61}BM. A *d*-spacing of 1.61–1.62 nm is retained, suggesting that P3HT domains are not denser. However, CCL values increased in ternary blends, highlighting the formation of longer-ordered donor-enriched crystallites. By the presence of a diffraction peak (100) in the in-plane profiles of P3HT and ternary layers (Figure S9), a face-on lamellar orientation of P3HT crystallites is also induced in solid films. However, the intense (010) diffraction peak in these in-plane profiles strengthens the edge-on orientation, which is even more prevalent for films annealed at 140 °C with a (100)/(010) ratio decreasing towards 1 in P3HT:PC_{61}BM:eh-IDTBR layers. The 2D-GIXRD measurements confirm the good incorporation of NFA molecules in BHJs, driving P3HT polymer chains to form enlarged ordered-donor domains.

Table 3. XRD data of neat P3HT layer, binary (P3HT:PC_{61}BM) and ternary (P3HT:PC_{61}BM:ITIC and P3HT:PC_{61}BM:eh-IDTBR) blends as a function of thermal annealing temperature.

Layer	Ratio	T (°C)	q_z ($Å^{-1}$)	d (nm)	CCL (nm)
P3HT		100	0.39	1.61	2.24
		140	0.39		2.07
P3HT:PC_{61}BM	1:1	100	0.39	1.61	2.27
		140	0.39		1.96
P3HT:PC_{61}BM:ITIC	0.85:1:0.15	100	0.38	1.62	2.88
		140	0.38		2.87
P3HT:PC_{61}BM:eh-IDTBR	0.85:1:0.15	100	0.38	1.62	3.01
		140	0.38		3.27

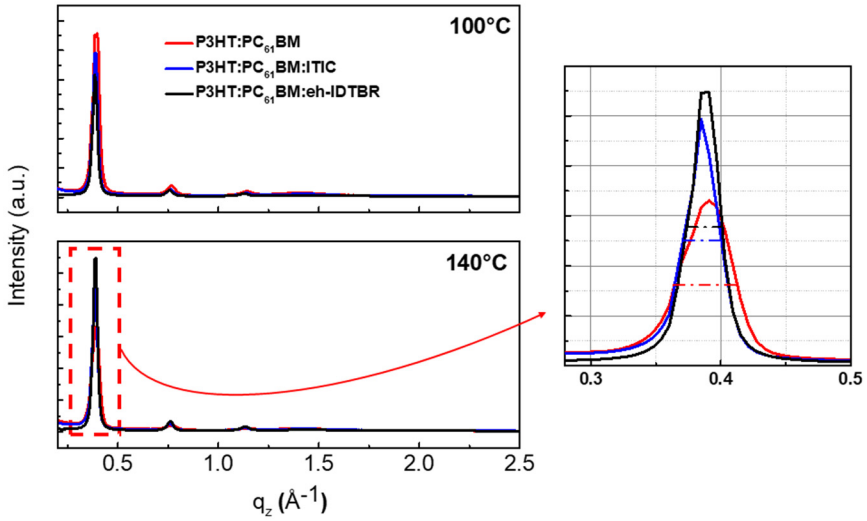

Figure 7. Out-of-plane profiles of binary and ternary layers as a function of thermal annealing temperature (100 °C and 140 °C). Zoom of (100) out-of-plan peaks at 140 °C where the dotted lines in the middle of the peaks indicate the FWHM.

4. Discussion

Through the introduction of ITIC or eh-IDTBR as a third component in the P3HT:PC_{61}BM host system, the three organic materials form a three-component cascade for charge transfer. In this energy cascade model, the energy levels of the third component are in between those of P3HT and PC_{61}BM and operate as charge relay material. From this simple standpoint, the third component facilitates the transport of holes to the anode and electrons to the cathode [33]. However, integrating new components can lead to significant changes in the morphology (both in the bulk and at the interfaces) of the binary blend, possibly altering charge transport and recombination paths and thereby affecting the charge extraction efficiency. When choosing a third component, an optimized compatibility must be established. Ideal chemical compatibility will allow the three components to be mixed in a sole solution to deposit a three-component photoactive layer without the need for multiple stacking. Physical compatibility means the ability of the materials to mix without substantially altering the crystallinity and texture of the pure phases.

A small amount of an NFA (ITIC or eh-IDTBR) is added into the binary P3HT:PC_{61}BM blends. Figure 5 depicts the evolution of electron and hole mobilities (μ_e, μ_h) and their ratio (μ_e/μ_h) together with PCE, FF and CCL values for neat PH3T, binary P3HT:PC_{61}B and ternary P3HT:PC_{61}BM:ITIC and P3HT:PC_{61}BM:eh-IDTBR blends as a function of thermal annealing (100 °C and 140 °C). The relationship between these parameters highlights the impact of the third component. The most significant effects are observed at the highest thermal annealing of 140 °C. Via the presence of 15 wt% of ITIC or eh-IDTBR in the blend, the nanomorphology of ternary blends thermally annealed at 140 °C improves the BHJ through high FF values and the extended CCL of P3HT. The incorporation of NFA molecules allows the polymer chains to move into a more crystalline configuration, which directly expels the fullerene for more efficient transport of the holes. As a consequence, through the good incorporation of NFA molecules in acceptor-enriched phases, electron transport is also enhanced. Through the concomitant increase of mobility values, the balanced mobility between holes and electrons is achieved in ternary blends annealed at 140 °C. All these positive improvements decrease the rate of charge recombination and improve charge transport and collection in the corresponding solar cells towards higher PCE values in ternary blends (see red-colored regions in Figure 5).

The addition of ITIC and eh-IDTBR, as a third component, to the P3HT:PC_{61}BM host blends is primarily intended to bring panchromaticity to the cell. Additionally, through the formation of an energy cascade, NFA molecules help with charge separation and ensure the effective suppression of recombination. ITIC and eh-IDTBR will also form an amorphous mixed phase with PC_{61}BM at photogenerating interfaces to ensure a higher voltage owing to the well-known voltage tuning of pseudo-binary blends. Away from the interface, however, crystalline phases are made of the main P3HT absorber, which enables efficient charge transport and reduced recombination.

5. Conclusions

The incorporation of a third NFA-based component, ITIC or eh-IDTBR, in the well-known P3HT:PC_{61}BM system has been successfully implemented. These two examples of ternary P3HT:PC_{61}BM:ITIC and P3HT:PC_{61}BM:eh-IDTBR blends suggest that the mixing of two acceptors in a ternary blend is not detrimental and is even favorable as the structural order is either unperturbed or even improved for enhanced charge collection upon the addition of ITIC or eh-IDTBR. These three materials exhibit an efficient physical compatibility to form a single three-component photoactive layer in which the third component includes the enhancement of the light-harvesting ability, the production of a spectrally extended photocurrent and the optimization of the morphology of the active layer via the formation of highly crystalline nanoscale P3HT domains. An alloy-like mixed phase between acceptors and P3HT donor polymer maximizes the probability of charge separation, where transport benefits from increased mobility values in 140 °C-annealed ternary BHJ layers. In this context, optical absorption, the alignment of energy levels, film morphology and

device physics are four key parameters for efficient ternary OPV devices. For the successful application of these ternary OPV devices, it will be crucial to further investigate device lifetime and identify limiting factors, such as air, irradiation, heat and mechanical stress.

Supplementary Materials: The following supporting information can be downloaded at https://www.mdpi.com/article/10.3390/electronics13091752/s1: Table S1: Intensity and wavelength of maximum absorption peaks for neat films of P3HT, $PC_{61}BM$, ITIC and eh-IDTBR; Table S2: Electron and hole mobility values determined via SCLC protocol; Figure S1: Absorption spectra of neat films depending on annealing temperature; Figure S2: Absorption spectra of binary P3HT:$PC_{61}BM$ films depending on annealing temperature; Figure S3: AFM images of neat films and ternary P3HT:$PC_{61}BM$:ITIC blend thermal annealed at 140 °C; Figure S4: Graph showing WCA on neat films, binary and ternary blends as a function of thermal annealing temperature; Figure S5: The 2D-GIXRD patterns of blends as a function of thermal annealing temperature; Figures S6–S8: The 2D-GIXRD patterns and corresponding out of plane profiles of $PC_{61}BM$, eh-IDTBR and P3HT layers as a function of thermal annealing temperature; Figure S9: In-plane profiles of P3HT and P3HT:$PC_{61}BM$:eh-IDTBR layers as a function of thermal annealing temperature.

Author Contributions: Conceptualization, Q.E. and C.V.-A.; methodology, Q.E. and C.V.-A.; validation, N.Y. and C.V.-A.; investigation, Q.E., H.S., M.e.A.K. and T.K.; writing—original draft preparation, C.V.-A.; writing—review and editing, C.V.-A.; supervision, G.Q., O.M., J.A. and C.V.-A.; project administration, C.V.-A.; funding acquisition, J.A. and C.V.-A. All authors have read and agreed to the published version of the manuscript.

Funding: This research was funded by the French Research Agency (project ANR-18-CE04-0007-04 named BELUGA and project ANR-22-CE06-0018 named MONOPOLY).

Data Availability Statement: The data are contained within the article.

Acknowledgments: C.V.A. and J.A. would like to thank F. Jandard and S. Lavandier from CINaM (Electronics and Instrumentation Division) for their assistance in building the OPD measurement facilities and developing the acquisition software. The synchrotron radiation experiments were performed at BL19B2 in SPring-8 with the approval of the Japan Synchrotron Radiation Research Institute (JASRI) (proposal No. 2021B1947, 2022A2069 and 2022A2063).

Conflicts of Interest: The authors declare no conflicts of interest.

References

1. Scharber, M.C.; Sariciftci, N.S. Efficiency of bulk-heterojunction organic solar cells. *Prog. Polym. Sci.* **2013**, *38*, 1929–1940. [CrossRef] [PubMed]
2. Lu, L.; Zheng, T.; Wu, Q.; Schneider, A.M.; Zhao, D.; Yu, L. Recent advances in bulk heterojunction polymer solar cells. *Chem. Rev.* **2015**, *115*, 12666–12731. [CrossRef] [PubMed]
3. Huang, Y.; Kramer, E.J.; Heeger, A.J.; Bazan, G.C. Bulk heterojunction solar cells: Morphology and performance relationships. *Chem. Rev.* **2014**, *114*, 7006–7043. [CrossRef] [PubMed]
4. Nelson, J. Polymer:fullerene bulk heterojunction solar cells. *Mater. Today* **2011**, *14*, 462–470. [CrossRef]
5. Kim, H.; Shin, M.; Kim, Y. Distinct annealing temperature in polymer: Fullerene: Polymer ternary blend solar cells. *J. Phys. Chem. C* **2009**, *113*, 1620–1623. [CrossRef]
6. Gasparini, N.; Salleo, A.; McCulloch, I.; Baran, D. The role of the third component in ternary organic solar cells. *Nat. Rev. Mater.* **2019**, *4*, 229–242. [CrossRef]
7. Doumon, N.Y.; Yang, L.; Rosei, F. Ternary organic solar cells: A review of the role of the third element. *Nano Energy* **2022**, *94*, 106915. [CrossRef]
8. Ameri, T.; Khoram, P.; Min, J.; Brabec, C.J. Organic ternary solar cells: A review. *Adv. Mater.* **2013**, *25*, 4245–4266. [CrossRef]
9. Bi, P.; Hao, X. Versatile ternary approach for novel organic solar cells: A review. *Sol. RRL* **2019**, *3*, 1800263. [CrossRef]
10. Zhang, Y.; Li, G. Functional third components in nonfullerene acceptor-based ternary organic solar cells. *Acc. Mater. Res.* **2020**, *1*, 158–171. [CrossRef]
11. Zhan, L.; Li, S.; Li, Y.; Sun, R.; Min, J.; Chen, Y.; Fang, J.; Ma, C.-Q.; Zhou, G.; Zhu, H.; et al. Manipulating charge transfer and transport via intermediary zlectron acceptor channels enables 19.3% efficiency organic photovoltaics. *Adv. Energy Mater.* **2022**, *12*, 2201076. [CrossRef]
12. Ma, R.; Yan, C.; Fong, P.W.-K.; Yu, J.; Liu, H.; Yin, J.; Huang, J.; Lu, X.; Yan, H.; Li, G. *In situ* and *ex situ* investigations on ternary strategy and co-solvent effects towards high-efficiency organic solar cells. *Energy Environ. Sci.* **2022**, *15*, 2479–2488. [CrossRef]

13. Kim, C.S.; Tinker, L.L.; Di Salle, B.F.; Gomez, E.D.; Lee, S.; Bernhard, S.; Loo, Y.-L. Altering the thermodynamics of phase separation in inverted bulk-heterojunction organic solar cells. *Adv. Mater.* **2009**, *21*, 3110–3115. [CrossRef]
14. Xu, X.; Zhang, G.; Yu, L.; Li, R.; Peng, Q. P3HT-based polymer solar cells with 8.25% efficiency enabled by a matched molecular acceptor and smart green-solvent processing technology. *Adv. Mater.* **2019**, *31*, 1906045. [CrossRef] [PubMed]
15. Lin, Y.; Wang, J.; Zhang, Z.-G.; Bai, H.; Li, Y.; Zhu, D.; Zhan, X. An Electron Acceptor Challenging Fullerenes for Efficient Polymer Solar Cells. *Adv. Mater.* **2015**, *27*, 1170–1174. [CrossRef] [PubMed]
16. Yuan, J.; Zhang, Y.; Zhou, L.; Zhang, G.; Yip, H.-L.; Lau, T.-K.; Lu, X.; Zhu, C.; Peng, H.; Johnson, P.A.; et al. Single-Junction Organic Solar Cell with over 15% Efficiency Using Fused-Ring Acceptor with Electron-Deficient Core. *Joule* **2019**, *3*, 1140–1151. [CrossRef]
17. Zhang, G.; Zhao, J.; Chow, P.C.Y.; Jiang, K.; Zhang, J.; Zhu, Z.; Zhang, J.; Huang, F.; Yan, H. Nonfullerene acceptor molecules for bulk heterojunction organic solar cells. *Chem. Rev.* **2018**, *118*, 3447–3507. [CrossRef] [PubMed]
18. Holliday, S.; Ashraf, R.S.; Wadsworth, A.; Baran, D.; Yousaf, S.A.; Nielsen, C.B.; Tan, C.H.; Dimitrov, S.D.; Shang, Z.; Gasparini, N.; et al. High-efficiency and air-stable P3HT-based polymer solar cells with a new non-fullerene acceptor. *Nat. Commun.* **2016**, *7*, 11585. [CrossRef] [PubMed]
19. Ben Dkhil, S.; Perkhun, P.; Luo, C.; Müller, D.; Alkarsifi, R.; Barulina, E.; Avalos Quiroz, Y.A.; Margeat, O.; Dubas, S.T.; Koganezawa, T.; et al. Direct correlation of nanoscale morphology and device performance to study photocurrent generation in donor-enriched phases of polymer solar cells. *ACS Appl. Mater. Interfaces* **2020**, *12*, 28404–28415. [CrossRef]
20. Eynaud, Q.; Avalos Quiroz, Y.A.; Koganezawa, T.; Sato, R.; Yoshimoto, N.; Margeat, O.; Ruiz, C.M.; Ackermann, J.; Videlot-Ackermann, C. Towards efficient NFA-based selective near-infrared organic photodetectors: Impact of thermal annealing of polymer blends. *J. Mater. Chem. C* **2023**, *11*, 9657–9669. [CrossRef]
21. Eynaud, Q.; El Amine Kramdi, M.; Kannampalli, V.; Koganezawa, T.; Yoshimoto, N.; Santinacci, L.; Ackermann, J.; Videlot-Ackermann, C. Towards air-stability of efficient filter-free band-selective organic photodetectors based on bulk heterojunction: Avoiding environmental degradation with atomic layer deposition encapsulation. *Adv. Energy Sustain. Res.* **2024**, 2300262. [CrossRef]
22. Blakesley, C.; Castro, F.A.; Kylberg, W.; Dibb, G.F.A.; Arantes, C.; Valaski, R.; Cremona, M.; Kim, J.S.; Kim, J.-S. Towards reliable charge-mobility benchmark measurements for organic semiconductors. *Org. Electron.* **2014**, *15*, 1263–1272. [CrossRef]
23. Fei, Z.; Boufflet, P.; Wood, S.; Wade, J.; Moriarty, J.; Gann, E.; Ratcliff, E.L.; McNeill, C.R.; Sirringhaus, H.; Kim, J.-S.; et al. Influence of backbone fluorination in regioregular poly(3-alkyl-4- fluoro)thiophenes. *J. Am. Chem. Soc.* **2015**, *137*, 6866–6879. [CrossRef] [PubMed]
24. Liu, H.-W.; Chang, D.-Y.; Chiu, W.-Y.; Rwei, S.-P.; Wang, L. Fullerene bisadduct as an effective phase-separation inhibitor in preparing poly(3-hexylthiophene)–[6,6]-phenyl-C61-butyric acid methyl ester blends with highly stable morphology. *J. Mater. Chem.* **2012**, *22*, 15586–15591. [CrossRef]
25. Szymanski, R.; Henry, R.; Stuard, S.; Vongsaysyn, U.; Courtel, S.; Vellutini, L.; Bertrand, M.; Ade, H.; Chambon, S.; Wantz, G. Balanced charge transport optimizes industry-relevant ternary polymer solar cells. *Sol. RRL* **2020**, *4*, 2000538. [CrossRef]
26. Ameri, T.; Min, J.; Li, N.; Machui, F.; Baran, D.; Forster, M.; Schottler, K.J.; Dolfen, D.; Scherf, U.; Brabec, C.J. Performance enhancement of the P3HT/PCBM solar cells through NIR sensitization using a small-bangap polymer. *Adv. Energy Mater.* **2012**, *2*, 1198–1202. [CrossRef]
27. Bristow, H.; White, A.J.P.; Wadsworth, A.; Babics, M.; Hamid, Z.; Panidi, J.; McCulloch, I. Impact of nonfullerene acceptor side chain variation on transistor mobility. *Adv. Electon. Mater.* **2019**, *5*, 1900344. [CrossRef]
28. Sun, Q.; Zhang, F.; Wang, J.; An, Q.; Zhao, C.; Li, L.; Teng, F.; Hu, B. A two-step strategy to clarify the roles of a solution processed PFN interfacial layer in highly efficient polymer solar cells. *J. Mater. Chem. A* **2015**, *3*, 18432–18441. [CrossRef]
29. Lv, R.; Chen, D.; Liao, X.; Chen, L.; Chen, Y. A thermally tetrafluorinated nonfullerene acceptor for well-performing alloy ternary solar cells. *Adv. Funct. Mater.* **2019**, *29*, 1805872. [CrossRef]
30. Pascual-San-José, R.; Rodríguez-Martínez, X.; Adel-Abdelaleim, R.; Stella, M.; Martínez-Ferrero, E.; Campoy-Quiles, M. Blade coated P3HT:non-fullerene acceptor solar cells: A high-throughput parameter study with a focus on up-scalability. *J. Mater. Chem. C* **2019**, *7*, 20369–20382. [CrossRef]
31. Li, C.; Li, M.; Ni, Z.; Guan, Q.; Blackman, B.R.K.; Saiz, E. Stimuli-responsive surfaces for switchable wettability and adhesion. *J. R. Soc. Interface* **2021**, *18*, 20210162. [CrossRef] [PubMed]
32. Avalos-Quiroz, Y.A.; Koganezawa, T.; Perkhun, P.; Barulina, E.; Ruiz, C.M.; Ackermann, J.; Yoshimoto, N.; Videlot-Ackermann, C. Exploring charge transport in high temperature polymorphism of ITIC derivatives in simple processed unipolar bottom contact organic field-effect transistor. *Adv. Electon. Mater.* **2022**, *8*, 2100743. [CrossRef]
33. Koppe, M.; Egelhaaf, H.J.; Dennler, G.; Scharber, M.C.; Brabec, C.J.; Schilinsky, P.; Hoth, C.N. Near IR sensitization of organic bulk heterojunction solar cells: Towards optimization of the spectral response of organic solar cells. *Adv. Funct. Mater.* **2010**, *20*, 338–346. [CrossRef]